EasyChair Preprint

№ 6698

Study of the Thermal Performance of an Industrial Alumina Chlorination Reactor Based on CPFD Simulation

Zahir Barahmand, Chameera Jayarathna and Chandana Ratnayake

September 26, 2021

Study of the Thermal Performance of Industrial Alumina Chlorination Reactor Based on CPFD Simulation

Zahir Barahmand[1] Chameera Jayarathna[2] Chandana Ratnayake[1,2]

[1] Department of Process, Energy and Environmental Technology, University of South-Eastern Norway
zbarahmand@gmail.com
[2] SINTEF Tel-Tek, SINTEF Industry, Porsgrunn, Norway

Abstract

As a part of the new sustainable aluminum production process under study, alumina chlorination plays a crucial role. The relevant process is an exothermic reaction in a fluidized bed reactor. The solid alumina reacts with chlorine and carbon monoxide and produces aluminum chloride and carbon dioxide as the main products. Then carbon dioxide can be separated efficiently. The optimum temperature for the alumina chlorination is 700℃. The reactor's temperature should be kept in the range of 650-850℃ (most preferably 700℃) because below that temperature range, the reaction rate drops, and above that range, the alumina (which usually is γ-alumina) transfers to other alumina types, which is not desirable for the purpose.

Extending other simulation studies by authors on alumina chlorination in an isothermal condition, the CPFD method has been utilized to thermal study and simulate the overall heat transfer of the system, including convective fluid to the wall, fluid to particle, and radiation heat transfer. Radial and axial heat transfer coefficient profiles at different levels show that almost all the heat should be transferred in the lower half of the reactor, making the design more challenging. At the steady-state, the range for the fluid temperature inside the reactor has been recorded 700-780℃.

Keywords: Heat transfer, fluidized bed reactor, alumina chlorination, exothermic reaction, Barracuda, radiation, thermal simulation, CPFD simulation

1 Introduction

The Hall-Héroult process used almost exclusively in the aluminum industry suffers from relatively high heat loss from the electrolytic cells and increased CO_2 emissions from the anodes, even though manufacturers have gradually improved their production processes (Kovács et al., 2020). In 2001, Jomar Thonstad, professor of Electrochemistry at the Norwegian university of science and technology (NTNU), and his colleagues, in their book (Thonstad, 2001), mentioned that "the Hall-Héroult process remains the only modern method of producing aluminum today, having withstood many attempts to replace it. No other mechanism seems to be threatening it for the next twenty years or so," and it has been 20 years now.

Alternative aluminum processing strategies have been under intense investigation due to the comparatively high energy usage and carbon footprint associated with anode consumption (Thonstad, 2001). In continuation of this, in 1973, an innovative process was introduced by Alcoa Corporation, and it had several advantages compared to the commonly used method (Hall-Héroult) at that time (*National Fuels and Energy Conservation Act, S. 2176*, 1973). Alcoa's process is based on the chlorination of processed aluminum oxide in a fluidized bed. The chlorination process has the advantages of being more compact and operating at a lower temperature than the Hall-Héroult process, normally 700°C as well as less carbon footprint.

During the last decades, fluidized bed reactors (FBR) have been used in a wide range of applications in the industry due to the inherited uniform thermal distribution through the reactor, high heat and mass transfer, and flexibility in operation in large-scale applications (Zhang & Wei, 2017). In a fluidized bed, solid particles are suspended by a stream of fluid that flows upward, causing the solid suspension to move fluidly (Alagha & Szentannai, 2020). Fluidized bed technology has become widely employed in power generation due to its superior mixing and heat transport characteristics (Basu, 2006; Scala, 2013), chemical (Kunii & Levenspiel, 1991; Yang, 2003), pharmaceutical industries (Almendros-Ibáñez et al., 2019; Miller et al., 2018), etc.

Heat transfer occurs either spontaneously or intentionally in many gas fluidized bed applications. Heat transfer may occur between the solid and gas phases, the two-phase mixture, a solid surface, or both (Yang, 2003). The fluidized chlorination of alumina, for example, is a process in which alumina particles are fluidized by an equimolar mixture of carbon monoxide and chlorine at 700 ℃. The exothermic chlorination of alumina at the particle surface raises particle temperature, which leads to natural heat transfer from the heated particles to the fluidizing gas mixture (Barahmand et al., 2021b). To keep the bed's overall energy balance (the reactor temperature should be kept around 700 ℃), heat must be transferred from the particle to the gas medium and then to a cooling surface,

such as heat exchanger tubes, reactor jacket, or any other cooling apparatus.

In the FBR, several heat transfer mechanisms could be identified, such as fluid convection, solid particle conduction or convection, and radiation (Nauman, 2001). Thermal diffusion (heat conduction), convection, and radiation are the three primary modes of heat transfer. These mechanisms may exist simultaneously, or one of them may predominate under particular circumstances (Fan & Zhu, 1998). These conduction and convection modes are similar to their fluid-based counterparts in terms of momentum transfer. Thermal radiation, a type of energy transport via electromagnetic waves, is regulated by a distinct set of principles and can even occur in a perfect vacuum. It should also be noted that due to the similarities of their governing equations, mass transfer and heat transfer (without radiation) may be compared.

Intraparticle heat transport is dominated by conductive heat transfer. Conductive heat transfer is essential for fluid heat transfer at low Reynolds number flow conditions (Tsotsas, 2019). In addition to heat conduction, thermal convection enhances heat transfer from a thermal surface exposed to a flowing fluid (Garcia-Gutierrez et al., 2020). In a bubbling fluidized bed, the convective heat transfer mechanism occupies the total heat transfer flux (Qiu et al., 2016). Natural convection in a gas-solid system is generally negligible, even though thermal convection generally comprises forced and natural convection (Fan & Zhu, 1998). In a thermally radiative condition, absorption, reflection, refraction, and diffraction have happened for an element in the system. Not only can the element transmit incoming radiative heat fluxes but also emits its radiative heat flux (Fan & Zhu, 1998). Gray bodies can represent most solid materials in gas-solid fluxes, including particles and pipe walls. The term *scattering* can describe several modes of radiative energy transmission (Filla et al., 1996).

In thermal studies, solids not only alter the size as a result of pyrolysis, but the rates of reactions and fluid temperatures can also be affected by solid surface areas, solid material types, and discrete solid temperatures (Snider et al., 2011). The particle phase can be modeled in a variety of ways utilizing discrete computational particles or components. Only a small number of particles can be calculated using the direct numerical solution and Lattice Boltzmann computations. The CPFD approach to simulating a reactive thermal fluid-solid flow is reported in the current manuscript. The multi-phase-particle-in-cell (MP-PIC) technique is used in the CPFD numerical methodology to calculate dense particle flows (Snider, 2001). The MP-PIC technique is a hybrid numerical approach that solves the fluid phase with an Eulerian computational grid and models the solids with Lagrangian computational particles (Snider et al., 2011).

The current simulation work aims to study heat transfer between reactive materials in an industrial FBR reactor (dedicated for alumina chlorination) and its wall. To maintain the pseudo-steady-state, the heat produced from exothermic reactions should be transferred outside the reactor (cooling). Further investigations are done on temperature gradient and its variations through the height of the reactor.

2 Energy balance

A flow reactor's thermal energy balance can be written in a reasonably general way as below,

$$\frac{dU}{dt} = \dot{H}_i - \dot{H}_e + \dot{W}_f + \dot{W}_V + \dot{Q}_r + \dot{Q}_T \qquad (1)$$

where, $\frac{dU}{dt}$ is the accumulation of energy, $\dot{H}_i$ and $\dot{H}_e$ are convective enthalpy of input and output streams, respectively, $\dot{Q}_r$ is the heat generated by the reaction, $\dot{Q}_T$ is the heat transferred to the environment[1] (radiation, convection, and conduction), $\dot{W}_V$ is added work associated with the volume change, and $\dot{W}_f \geq 0$ is the friction work.

By neglecting volume and friction work, equation (1) can be simplified as,

$$\frac{dU}{dt} = \dot{H}_i - \dot{H}_e - \dot{Q}_r - \dot{Q}_T \qquad (2)$$

In thermodynamics, one of several energy expressions is *enthalpy H*, which simply is defined as (Lie, 2019),

$$H \triangleq U + PV \qquad (3)$$

Working on the left-hand side of equation (2) results,

$$U = H - PV \Rightarrow \frac{dU}{dt} = \frac{d(H - PV)}{dt} = \frac{dH}{dt} - P\frac{dV}{dt} - V\frac{dP}{dt} = \frac{dH}{dt}$$

$$H = m\widehat{H} \Rightarrow \frac{dH}{dt} = \frac{d\left(m\widehat{H}\right)}{dt} = m\frac{d\widehat{H}}{dt} + \widehat{H}\frac{dm}{dt} = m\frac{d\widehat{H}}{dt}$$

$$\frac{dU}{dt} = \frac{d}{dt}(\hat{\rho}V) \qquad (4)$$

In the same manner, by simplification of the right-hand side, the thermal energy balance is turned to,

$$\frac{d}{dt}\left(\hat{\rho}V\widehat{H}\right) = \dot{V}_{in}\rho_{in}\widehat{H}_{in} - \dot{V}_{out}\rho_{out}\widehat{H}_{out} + \hat{r}_A V\Delta\widehat{H}_r + \dot{Q}_r - \dot{Q}_T \qquad (5)$$

This is an integral balance that can be applied to the whole system. The enthalpies are defined relative to a

[1] This terms is positive when the heat leaves the control volume and includes all heat transport mechanisms

reference temperature (T_{ref}). The temperature would commonly be used to replace the enthalpy expressions.

$$H = \int_{T_{ref}}^{T} C_p \qquad (6)$$

Where, C_p is the average specific heat capacity for the entire reactant mixture. Taking the thermodynamics convenient into account, for exothermic reactions $\Delta H_r < 0$. The heat-generation expression refers to the net effect of all reactions where there are several reactions. As a consequence, the $\Delta H_r r$ expression is an implicit summation of all m potential reactions (Nauman, 2001):

$$\Delta H_r r = \sum_{Reactions} (\Delta H_r)_i (r)_i = \sum_{i=1}^{m} (\Delta H_r)_i (r)_i \qquad (7)$$

3 Heat Transfer Mechanisms

Barracuda® can quantify temperature gradients within the model due to initial particle and fluid temperatures, boundary state temperatures, thermal walls, or chemical reactions. In the computational particle fluid dynamics (CPFD) simulation, the following mechanisms can be studied by Barracuda® (*Barracuda User Manual*, 2021): the convective fluid-to-wall heat transfer, which includes lean-phase and dense-phase heat transfer, fluid-to-particle heat transfer, and radiation, including P-1 model for thermal radiation and Wall to particle radiation.

3.1 Convective fluid-to-wall heat transfer

The sum of the coefficients for a lean and dense phase in the fluidized bed is often used to indicate the effective heat transfer coefficients as below (Yang, 2003),

$$h_{fw} = h_l + f_d h_d \qquad (8)$$

$$f_d = 1 - e^{-10(\theta_p/\theta_{cp})} \qquad (9)$$

where, h_{fw} is the local fluid-wall heat transfer coefficient, h_l is a combination of contributions from a lean gas phase heat transfer coefficient, θ_{cp} is the close pack value fraction, θ_p is the particle volume fraction at the wall, and a dense particle phase's coefficient, h_d. The fluid-to-wall heat transfer coefficient is weighted by the function f_d , which is the fraction of contact time by the dense particle phase. The time fraction of dense phase contact, f_d is a function of the particle volume fraction at the wall.

For the heat transfer in a lean phase, the general form of heat transfer coefficient is,

$$h_l = \left(\left(c_0 Re_L^{n_1} Pr^{n_2} + c_1 \right) \frac{k_f}{L} + c_2 \right) \qquad (10)$$

where, c_0, c_1, c_2, n_1, and n_2 are adjustable model parameters, k_f is the thermal conductivity of the fluid, L is the cell length, and Re_L is the Reynolds number, and Pr is the Prandtl number (Bergman et al., 2011).

In these simulations, the following default lean phase heat transfer coefficient, based on the correlation of Douglas and Churchill (Yang, 2003), has been used.

(c_0 = 0.46, c_1 = 3.66, c_2 = 0.0, n_1 = 0.5, and n_2 = 0.33)

In the dense phase, the general form of the heat transfer coefficient is as below,

$$h_d = \left(c_0 Re_L^{n_1} \right) \frac{k_f}{d_p} \qquad (11)$$

where, d_p is the particle diameter.

Similarly, the following default dense phase heat transfer coefficients (Yang, 2003) have been used in the simulation.

(c_0 = 0.525, n_1 = 0.75)

3.2 Fluid-to-particle heat transfer

The fluid-to-particle heat transfer coefficient is used to describe heat transmission between the fluid and particle phases.

$$h_l = \left(\left(c_0 Re_p^{n_1} Pr^{0.33} + c_1 \right) \frac{k_f}{d_p} + c_2 \right) \qquad (12)$$

where, the Reynolds number and Prandtl number are defined as,

$$Re_L = \frac{\rho_f |U_f - U_p| d_p}{\mu_f} \quad , \quad Pr = \frac{\mu_f c_{p,f}}{k_f} \qquad (13)$$

where, U_f is the fluid velocity, U_p is the particle velocity, ρ_f is the fluid density, μ_f is the fluid's dynamic viscosity, and $c_{p,f}$ is the fluid heat capacity.

In a fluidized bed, when the Reynolds number is less than 20, the Nusselt number for a single sphere is typically higher than the particle Nusselt number. A single sphere in a quiescent fluid has a Nu_p = 2, representing the limit of conductive heat transfer. On the other hand, the bubbling phenomena cause the observed magnitude of Nu_p to be less than 2 in a fluidized bed. Low Reynolds numbers correspond to tiny particle beds (small d_p and U_p) with entrained particles clouding the bubbles. This reduces the efficiency of particle-gas interaction below the assumed plug flow level, resulting in lower Nu_p values. As particle diameter rises (coarse particle beds), the "bubbles" become less cloudy, and gas-particle interaction improves.

Barracuda® uses a correlation for fluid-to-particle heat transfer coefficient dependent on McAdams' correlation to capture fluid-to-particle heat transfer in a fluidized bed (Fan & Zhu, 1998).

(c_0 = 0.37, c_1 = 0.1, c_2 = 0.0, and n_1 = 0.6)

3.3 Radiation model

3.3.1 P-1 radiation model:

This model, which is the simplest case of the more general P-N model (*ANSYS FLUENT User Guide*, 2021), addresses the heat transfer, where thermal radiation between particles, particles and fluid, particles and thermal walls, and fluid and thermal walls are taken into account. In the P-1 radiation model, the incident radiation transfer equation is:

$$\nabla \cdot (\Gamma \nabla G) + 4\left(an^2\sigma T^4 + E_p\right) - \left(a - a_p\right)G = 0 \qquad (14)$$

where, Γ is the diffuse radiation coefficient, G is the incident radiation to be solved, a is the absorption coefficient of the fluid mixture, n is the refractive index of the fluid mixture, σ is the Stefan-Boltzmann constant, T is the fluid temperature in units of K, E_p is equivalent emission of the particles, and a_p is the equivalent particle absorption coefficient.

By defining a thermal boundary condition, the Marshak boundary condition (Elshin et al., 2018) is used for the radiative heat flux at the thermal wall (q_w) as the following:

$$-q_w = \Gamma_w\left(\frac{\partial G}{\partial n}\right) = \frac{\varepsilon_w}{2(2-\varepsilon_w)}\left(4\sigma T_w^4 - G_w\right) \qquad (15)$$

$$\Gamma = \frac{1}{3\left(a + a_p + \sigma_f + \sigma_p\right)} \qquad (16)$$

Where, ε_w is the emissivity of the thermal wall, w is subscript for thermal wall, σ_f is equivalent fluid scattering coefficient, and σ_p is identical particle scattering factor.

3.3.2 Particle to Wall Radiation:

The model is only used under thermal wall boundary conditions and only considers radiation between a thermal wall and the particle phase and ignores radiative heat transfer between particles-walls or wall-fluid. The radiation between a thermal wall cell and nearby particles (q_{wp}) is calculated as (*Barracuda User Manual*, 2021),

$$q_{wp} = A_w F_{wp} \varepsilon_{wp} \sigma \left({T_w}^4 - {\bar{T}_p}^4\right) \qquad (17)$$

$$\Gamma \varepsilon_{wp} = \left(\frac{1}{\bar{\varepsilon}_p} + \frac{1}{\varepsilon_w} - 1\right) \qquad (18)$$

where, A_w is the area of the thermal wall, F_{wp} is a calculated view factor, ε_{wp} is the effective emissivity between the wall and the particles in a cell, T_w is the temperature of the wall, $\bar{T}_p$ is the mass-weighted average temperature of particles in a cell, and $\bar{\varepsilon}_p$ is the volume-weighted average of particle emissivity.

4 CPFD simulations

The CPFD simulations are based on the particle size distribution and reaction kinetics (pure γ-alumina chlorination) in an isothermal condition at 700℃ (Barahmand et al., 2021b). The geometry (cylindrical reactor with extended section) and other operational conditions (Barahmand et al., 2021a) for the pure γ-alumina chlorination. In Barracuda®, the thermal wall of a model applies a user-defined temperature to the reactor wall. Energy can be transferred via the reactor wall depending on the temperature in between the wall and the fluid near the wall. The model has been simulated under the following operating condition (Table 1):

Table 1. Reactor's Operating Condition

Number of cells in setup grid:	65000
Bed aspect ratio (H/D)	1.8
Wall temperature	973.15 K
Reactor initial temperature:	973.15 K
Outlet pressure:	1.5 bars
Particle diameter:	Distribution[2]
Particle density (envelope):	2100 kg/m^3
Particle sphericity	0.7
Initial bed void fraction	0.44
Fluidization regime	Bubbling

The alumina chlorination reaction is a rapid and exothermic reaction that mainly occurs at the bottom of the reactor (Barahmand et al., 2021b). As a result, the generated heat will not be distributed homogeneously through the entire height of the particle bed. Therefore, the surface area of the reactor has been divided into 7 different sections, as shown in Figure 1

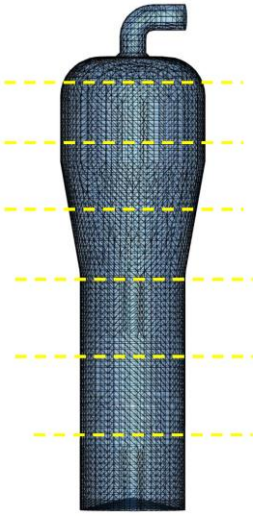

Figure 1. Reactor geometry and thermal-wall sections

[2] Based on (Barahmand et al., 2021b) with the average diameter of 98 microns.

5 Result and discussion

Due to a lack of information about the reactor wall emissivity, the heat transfer has been studied in three different cases. The first case is in the absence of radiation (emissivity = 0). In the second simulation, maximum possible radiation (emissivity = 1) has been set into the calculations, and in the last step, a relatively high emissivity (0.85) has been used.

5.1 Thermal model without radiation

The thermal simulations need much more time to reach pseudo-steady-state. Figure 2 shows the average fluid temperature distribution inside the reactor (middle cross-section). It seems like the local temperature is somewhat evenly distributed at the bottom part of the bed. The temperature at the bottom of the reactor is the highest since the reaction conversion is very high in that area.

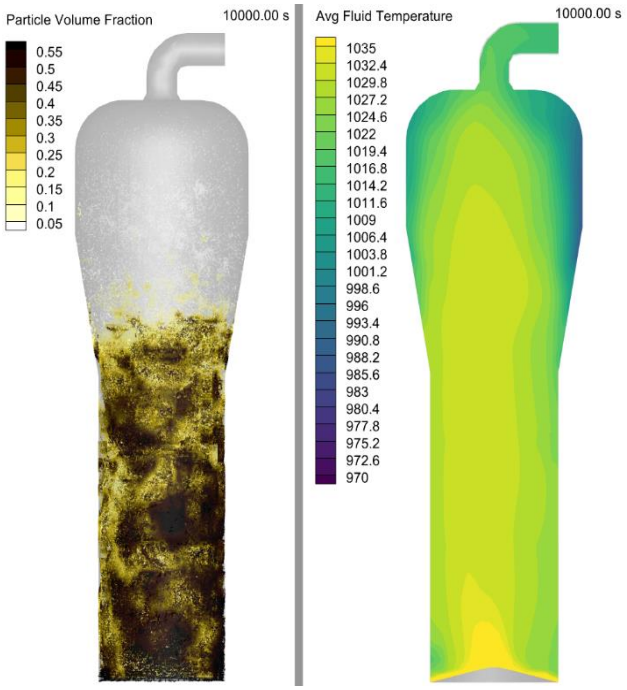

Figure 2 Particle distribution (left), and temperature distribution (right) at steady-state.

Figure 3 shows the heat transfer through the wall of the reactor. It seems it is necessary to transfer 1.56 MW of heat through the reactor wall at pseudo-steady-state to keep the reactor wall at 700℃. Theoretically, the heat duty transferred through the wall is not equally distributed. Table 2 gives the information about the heat transfer rate in different reactor sections in Figure 1. Starting from bottom to top, the sections are named from 1 to 7. Most of the heat leaves the reactor through the bottom half due to high energy generation from the exothermic chlorination reaction in the specific area.

Figure 4 illustrates the average fluid temperature in different sections of the reactor. Comparing figures 2 and 4 confirms that the fluid temperature inside the reactor is almost gradually decreasing from bottom to top. The highest recorded temperature is 792℃, and the average fluid temperature leaving the system is about 744℃.

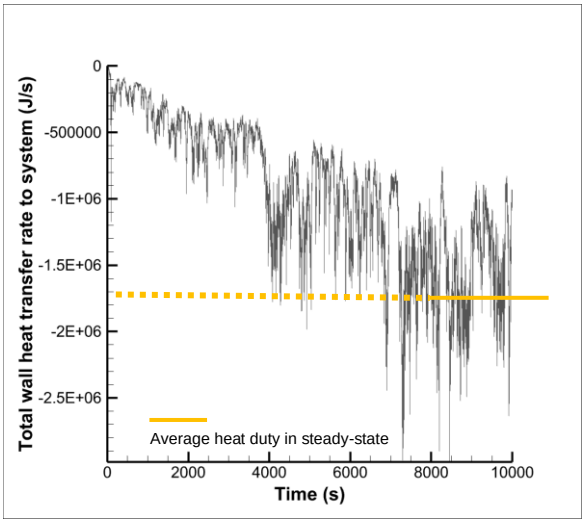

Figure 3. Overall heat transfer through the reactor wall

Table 2 Heat transfer in different sections

Section	Heat Transfer (MW)	(%) of total
1	0.22	14.2
2	0.41	26.2
3	0.61	39
4	0.26	16.6
5	0.31	2
6	0.016	1
7	0.013	< 1

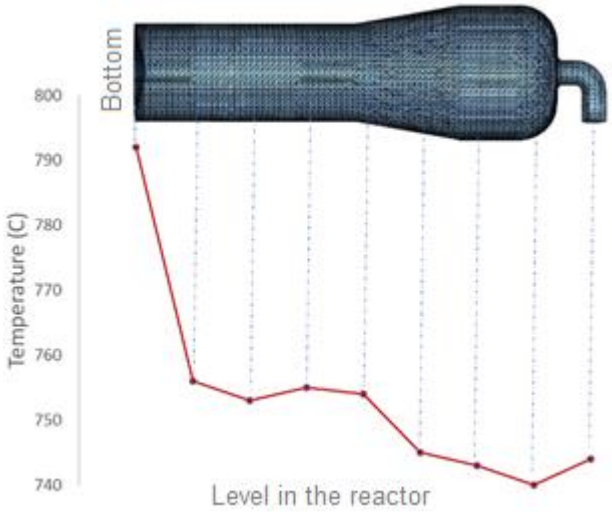

Figure 4. The fluid average temperature profile in different heights

5.2 Thermal model with radiation

5.2.1 Radiation (emissivity = 1)

By activating the P-1 model with maximum possible emissivity, the overall heat transfer through the reactor wall increases significantly. In this case, the overall heat transfer is 2 MW, almost 30 % higher than the heat transfer with no radiation (Figure 5). The portion of the convective mode is 29 % by 0.58 MW, and radiative heat transfer is 71 % by 1.4 MW (see Figure 6). In the current simulation, radiation is the dominant heat transfer mechanism.

Table 3 gives the overall view of heat transfer in the different sections of the reactor. Convective heat transfer has not been observed at the three upper sections of the reactor. The average fluid temperature in the middle vertical cross-section of the reactor is given in Figure 7. The fluid temperature is considerably lower because of the higher heat transfer (compared to the case with no radiation).

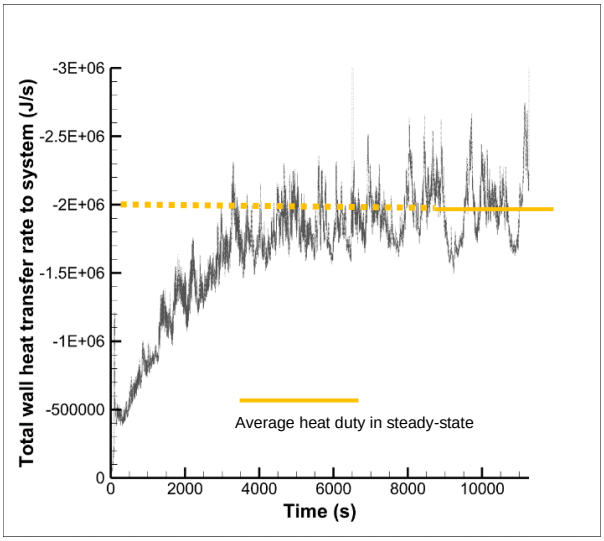

Figure 5 Reactor's overall heat transfer with maximum radiative heat transfer.

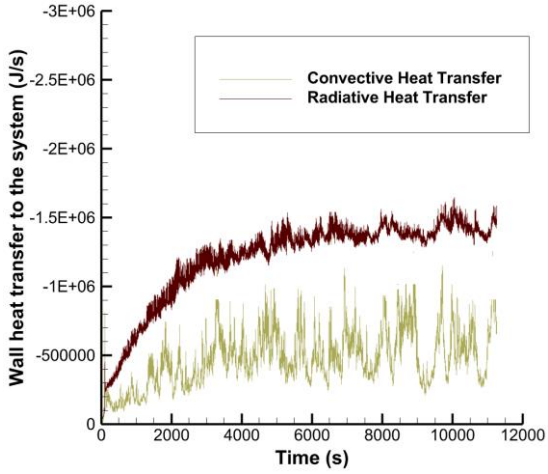

Figure 6. Convective and radiative heat transfer in the reactor (max emissivity)

Table 3. Convective and radiative Heat transfer in different sections of the reactor

Section	Convection		Radiation	
	Heat Transfer (kW)	(%)	Heat Transfer (MW)	(%)
1	92.4	16	264.8	19
2	163	28	240.6	17
3	224.9	39	266	19
4	90.3	16	180.4	13
5	6	1	192.5	14
6	2.9	< 1	224.3	16
7	2.1	~0	46.1	3

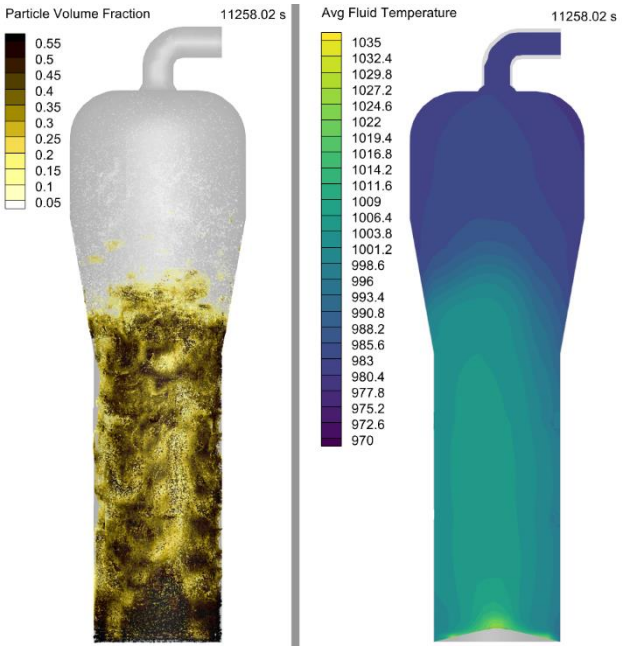

Figure 7. Particle distribution (right), and temperature distribution (left) in steady-state.

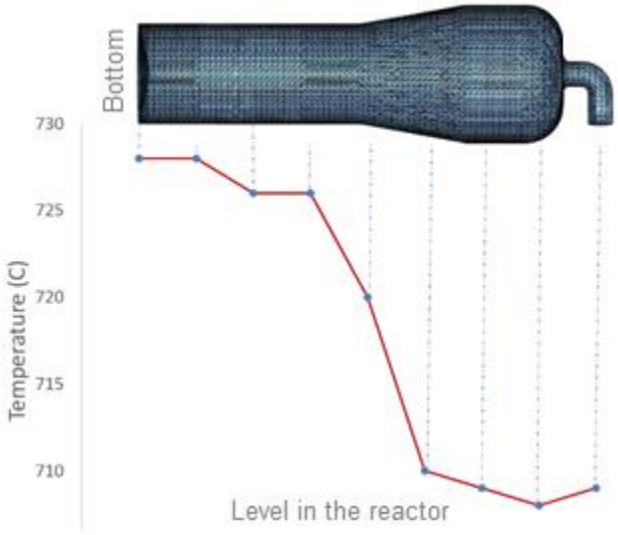

Figure 8. The fluid average temperature profile in different heights

Figure 8 illustrates the average fluid temperature in different sections of the reactor. The reactor temperature distribution can be divided mainly into three areas. The temperature in the first and the last three sections are almost constant. Nevertheless, in the middle section (4th), the reactor experienced a 20 ℃ temperature drop which can easily be observed in Figure 7. The average fluid temperature in the outlet is 709 ℃ which is very close to the desired temperature.

5.2.2 Radiation (emissivity = 0.85)

In sections 5.1 and 5.2.1, the extreme modes for the radiation (emissivity 0 and 1) have been investigated. In the last step, the emissivity is set to 0.85. The average overall heat transfer is 1.94 MW (Figure 9) which is 2.5 percent lower than the case with the maximum emissivity.

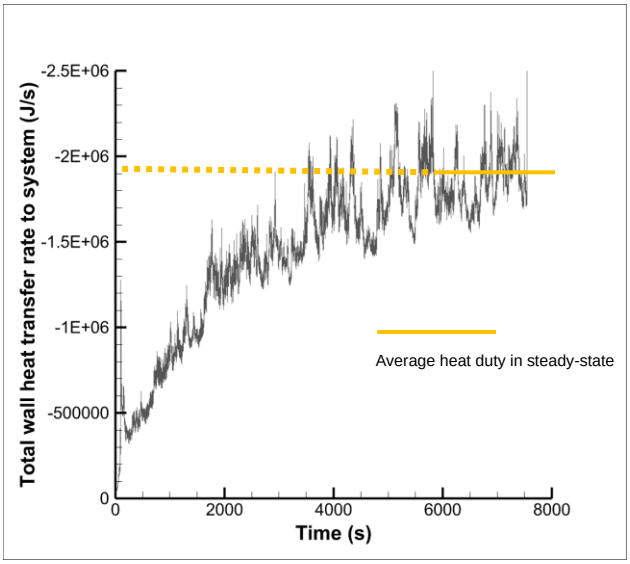

Figure 9. Reactor's overall heat transfer with maximum radiative heat transfer.

Table 4. Convective and radiative Heat transfer in different sections of the reactor

	Convection		Radiation	
Section	Heat Transfer (KW)	(%)	Heat Transfer (MW)	(%)
1	879	15	241.4	18
2	141.2	24	214.5	16
3	229.6	39	242.1	18
4	110.7	19	178.5	13
5	8	1	204.3	15
6	3.9	< 1	226.3	17
7	2.9	< 1	46	3

As expected, change in emissivity shows no effect on the convective heat transfer. The radiative heat transfer has been dropped to 1.35 MW. As seen in Table 4, the portion on each heat transfer mechanism in the different sections is almost the same as before. The average Outlet temperature has been recorded at 711℃ in comparison with 709℃ in the previous case.

To compare the heat duty calculated by the CPFD method, the reaction has been simulated in Aspen Plus® using the Gibbs reactor. A Gibbs reactor is a reactor that uses equilibrium processes to minimize the Gibbs free energy (Haydary, 2018). The Gibbs reactor simulation gave the 1.6 MW, which is slightly higher than the heat transfer in the absence of radiation and much lower than the cases with radiation. Several reasons may cause this variation, such as the difference in enthalpy value or heat formation in the libraries and different conditions in the outlet (because of the system's dynamics in CPFD simulation).

The enthalpy equation is used to explain energy. Energy transport in the fluid phase and energy transfer from the solid phase is described by energy conservation. Using a turbulent Prandtl number approximation, the turbulent thermal diffusion is derived from eddy conductivity. For each gas species, a transport equation is solved. Particle chemistry transfers mass and energy between solid and fluid phases. The enthalpy for each gas species includes the heat of formation from breaking and establishing chemical bonds.

6 Conclusion

Design an exothermic reactor with an efficient heat transfer performance is probably the most critical task from an engineering perspective. The efficiency of the reaction is highly affected by temperature. The CPFD method is applied to an industrial alumina chlorination reactor. The alumina chlorination calculation is three-dimensional, with chemistry in a large industrial hot reactor. The CPFD method provided a chlorination solution to 10000 seconds and took 47 days computation time on a single Intel Xeon E5 computer.

The Gibbs reactor simulation in Aspen Plus® shows lower heat transfer than thermal analysis by CPFD simulation. In CPFD simulation, at the steady-state, the reactor temperature range is 744-792℃ in the case with emissivity equal to 0, 709-728℃ for the case with the maximum emissivity, and 711-730℃ in the case with emissivity equal to 0.85. The possibility of having higher radiation by using the material with high emissivity helps to reach more heat transfer and lower temperature in the reactor. As a result, less cooling duty will be needed. For future studies, it is suggested to validate the model with other computational or experimental studies. Moreover, the mesh convergence test can help future studies find the best mesh size for the model.

References

M. Alagha and P. Szentannai. Analytical review of fluid-dynamic and thermal modeling aspects of fluidized beds for energy conversion devices. *International Journal of Heat*

and Mass Transfer, *147*, 118907, 2020. doi:10.1016/j.ijheatmasstransfer.2019.118907

J. Almendros-Ibáñez, M. Fernández-Torrijos, M. Díaz-Heras, J. Belmonte, and C. Sobrino. A review of solar thermal energy storage in beds of particles: Packed and fluidized beds. *Solar Energy*, *192*, 193–237, 2019. doi:10.1016/j.solener.2018.05.047

ANSYS FLUENT User Guide. 2021. https://www.afs.enea.it/project/neptunius/docs/fluent/html/th/node112.htm

Z. Barahmand, C. Jayarathna, and C. Ratnayake. CPFD simulations on a chlorination fluidized bed reactor for aluminum production: An optimization study. *In proceedings - 1st SIMS EUROSIM Conference on Modelling and Simulation*, Finland, 2021a.

Z. Barahmand, C. Jayarathna, and C. Ratnayake. The effect of alumina impurities on chlorination in a fluidized bed reactor: A CPFD study. *In proceedings - 1st SIMS EUROSIM Conference on Modelling and Simulation*, Finland, 2021b.

Barracuda User Manual. 2021. CPFD Software. https://cpfd-software.com/

P. Basu. *Combustion and Gasification in Fluidized Beds*. CRC Press, 2006.

T. Bergman, F. Incropera, D. DeWitt, and A. Lavine. *Fundamentals of Heat and Mass Transfer*. John Wiley & Sons, 2011.

A. Elshin, K. Muraveva, A. Borisenko, and A. Kalutik. Mark and Marshak boundary conditions in surface harmonics method. *Journal of Physics: Conference Series*, 2018. doi:10.1088/1742-6596/1133/1/012017

L. Fan, and C. Zhu. *Principles of Gas-Solid Flows*. Cambridge University Press, 1998.

M. Filla, A. Scalabrin, and C. Tonfoni. Scattering of thermal radiation in the freeboard of a 1 MWt fluidized bed combustion with coal and limestone feeding. *Symposium (International) on Combustion*, 26(2), 3295–3300, 1996. doi:10.1016/S0082-0784(96)80176-7

L. Garcia-Gutierrez, F. Hernández-Jiménez, E. Cano-Pleite, and A. Soria-Verdugo. Experimental evaluation of the convection heat transfer coefficient of large particles moving freely in a fluidized bed reactor. *International Journal of Heat and Mass Transfer*, *153*, 119612, 2020. doi:10.1016/j.ijheatmasstransfer.2020.119612

Haydary. (2018). Reactors. In *Chemical Process Design and Simulation* (pp. 101–124). John Wiley & Sons, Ltd. https://doi.org/10.1002/9781119311478.ch5

A. Kovács, C. Breward, K. Einarsrud, S. Halvorsen, E. Nordgård-Hansen, E. Manger, A. Münch, and J. Oliver. A heat and mass transfer problem for the dissolution of an alumina particle in a cryolite bath. *International Journal of Heat and Mass Transfer*, *162*, 120232, 2020. https://doi.org/10.1016/j.ijheatmasstransfer.2020.120232

D. Kunii and Levenspiel. *Fluidization Engineering*. Butterworth-Heinemann, 1991.

B. Lie. *Modeling of Dynamic Systems* [Unpublished book], 2019.

D. Miller, C. Pfutzner, and G. Jackson. Heat transfer in counter-flow fluidized bed of oxide particles for thermal energy storage. *International Journal of Heat and Mass Transfer*, *126*, 730–745, 2018. doi:10.1016/j.ijheatmasstransfer.2018.05.165

National Fuels and Energy Conservation Act, S. 2176. U.S. Government Printing Office, 1973.

B. Nauman, B. *Handbook of Chemical Reactor Design, Optimization, and Scaleup*. McGraw-Hill Professional, 2001. doi:10.1036/9780071395588

K. Qiu, F. Wu, S. Yang, K. Luo, K. Luo, and J. Fan. Heat transfer and erosion mechanisms of an immersed tube in a bubbling fluidized bed: A LES–DEM approach. *International Journal of Thermal Sciences*, 100, 357–371, 2016. https://doi.org/10.1016/j.ijthermalsci.2015.10.001

F. Scala, F. *Fluidized Bed Technologies for Near-Zero Emission Combustion and Gasification* (1st edition). Woodhead Publishing, 2013.

D. Snider. An Incompressible Three-Dimensional Multiphase Particle-in-Cell Model for Dense Particle Flows. *Journal of Computational Physics*, *170*(2), 523–549, 2001. doi:10.1006/jcph.2001.6747

D. Snider, S. Clark, P. & O'Rourke. Eulerian–Lagrangian method for three-dimensional thermal reacting flow with application to coal gasifiers. *Chemical Engineering Science*, 66(6), 1285–1295, 2011. doi:10.1016/j.ces.2010.12.042

J. Thonstad. *Aluminium Electrolysis: Fundamentals of the Hall-Héroult Process*. Aluminium-Verlag, 2001.

E. Tsotsas. Particle-particle heat transfer in thermal DEM: Three competing models and a new equation. *International Journal of Heat and Mass Transfer*, 132, 939–943, 2019. https://doi.org/10.1016/j.ijheatmasstransfer.2018.12.090

W. Yang. *Handbook of Fluidization and Fluid-Particle Systems*. CRC Press, 2003.

Y. Zhang and Q. Wei. CPFD simulation of bed-to-wall heat transfer in a gas-solids bubbling fluidized bed with an immersed vertical tube. *Chemical Engineering and Processing: Process Intensification*, 116, 2017. doi:10.1016/j.cep.2017.03.007